

Hot electrons and singlet-fission dark excitons modulate strong-coupling conditions in metal-organic optical microcavities

Pavel V. Kolesnichenko,^{*,†,‡} Manuel Hertzog,[†] Felix Hainer,^{†,‡} Oskar Kefer,^{†,‡}
Jana Zaumseil,[†] and Tiago Buckup^{*,†,‡}

[†]*Physikalisch-Chemisches Institut, Ruprecht-Karls-Universität Heidelberg, Heidelberg,
69120, Heidelberg, Germany*

[‡]*Institute for Molecular Systems, Engineering and Advanced Materials,
Ruprecht-Karls-Universität Heidelberg, 69120, Heidelberg, Germany*

E-mail: pavel.kolesnichenko@alumni.uni-heidelberg.de; tiago.buckup@pci.uni-heidelberg.de

Abstract

Polaritons, formed as a result of strong mixing between light and matter, are promising for numerous applications including organic solar cells, optical logic gates, and qubits. In low-Q organic optical microcavities, polaritonic signatures due to strong hybridization between photons and Frenkel excitons were found to decay together with the dynamics of dark excitons. A conundrum, however, remained whether dark excitons modulate exciton-photon coupling strength. It also remained unclear how dark excitons in the organic layer and hot electrons in the metal layers contribute to shaping the long-lived optical response at the energies of the hybrid states. Here, we identified that due to delocalization of polaritons over both organic and metal layers, they are sensitive to the effects of both dark excitons and hot electrons. We observed that the dynamics of dark excitons modulate exciton-photon strong coupling (Rabi energy). The role of metal layers is to contribute absorptive components near the energies of the polaritonic branches; contributions from hot electrons have also been detected. These and other mechanistic insights into the dynamics of strong-coupling conditions were supported by theoretical analysis based on non-Hermitian Hamiltonian mechanics, axially-resolved transfer-matrix simulations, global analysis of pump-probe spectra, and statistical correlation analysis. The developed methodology can be applied to other microcavity structures. Our findings pave the way for disentangling pure polaritonic effects from other excitations in organic and metal layers, with the ultimate aim of achieving photonic control over photophysical and photochemical processes.

Keywords

microcavity, optical cavity, photonics, spectroscopy, pump-probe, reflectance, polaritons, exciton-polaritons, strong coupling, hot electrons, metal layer

Introduction

Exciton-polaritons are hybrid quasi-particles which are formed as a result of strong light-matter interactions and inherit properties of both matter (excitons) and light (photons). They are promising for numerous applications such as terahertz sources and detectors,¹ low-threshold lasers,² all-optical transistors,³ refractive index sensors,⁴ organic solar cells,⁵ spatial light modulators,⁶ and qubits.⁷ On a more fundamental level, they have been used in studies of Bose-Einstein condensates,⁸ superfluids,⁹ and acoustic black holes,¹⁰ only to mention a few.

Strong coupling of light to matter (excitons) and related phenomena have been commonly studied using Wannier-Mott excitons in the active (semiconductor) layer of optical microcavities. More recently, organic matter has gained popularity because it can provide large density of Frenkel excitons with large binding energies allowing investigations of polaritonic phenomena even with low-Q microcavities and at room temperature.^{11–17} This has allowed the observation of such polariton-enhanced phenomena as, for example, super-absorption for energy storage,¹⁸ enhanced photoluminescence for lasing applications,¹⁹ and, for optoelectronic applications, enhanced energy-transfer through heterojunctions,²⁰ enhanced singlet fission²¹ and μ s-long lifetime of lower polariton.²² The scenarios of polariton-assisted enhancement of useful effects, however, may not always occur.^{21,23–25} Thus, for example, strong coupling of surface plasmons to chromophore-acceptors may not result in mesoscale energy transfer,²³ and that triplet yield from singlet fission can decrease either through the photonic leakage of polaritonic states,²¹ or, when mediated by conical intersection, due to poorer Franck-Condon overlap emerging in the hybrid system.²⁵

Recent time-resolved experiments aiming at revealing the effects of strong coupling on singlet fission in low-Q organic microcavities also showed no enhancement of triplet formation yield.²⁴ At the same time, strong dispersive signatures of exciton-polaritons lasted nearly as long as the lifetime of triplet excitons. This has been attributed to the very fast decay of polaritons to the manifold of long-lived dark states before any photonic leakage occurred.^{24,26}

Dispersive lineshapes of polaritons were attributed to changes in the number of coupled molecules and the effective refractive index of the cavity.²⁴ Even when inducing changes of optical properties of the metal layers alone (with no dark excitons involved) using infrared photons, it was still possible to observe polaritonic signatures near the main exciton resonance in the visible.²⁷ In these experiments, the observed signals represented rather strong-coupling conditions than long-lived polaritons¹⁶ since there was no real pump-induced population of polaritonic states. In this case, however, Rabi energy quantifying strong coupling was not observed to be sensitive to changing strong coupling conditions, which remained to be established. These results, nevertheless, suggest that in general the strong optical response at the energies of hybrid modes can contain information on carrier dynamics in both active and metal layers of the cavity. Their disentanglement, however, remained a challenge as well as their manifestation in the nonlinear optical response unclear.

Here, using TIPS-Pentacene (TIPS-PEN) in the active layer, we disentangle main contributions to changing strong-coupling conditions in low-Q all-metal optical microcavities. In such structures, polaritons were found to be delocalized over both organic and metal layers inheriting information on the dynamics of dark excitons and hot electrons, respectively, modulating strong coupling. First, strong coupling is quantified through the Rabi energy that is demonstrated to be strongly correlated with the dynamics of dark excitons undergoing singlet fission in the organic layer. Next, dark excitons are shown to contribute additional phase offsets to polaritonic resonances responsible for changes of the Rabi energy. Further, thin metal layers are found to contribute significant absorptive components near the energies of polaritonic branches further shaping nonlinear optical response. Finally, contributions from hot electrons were unambiguously identified with the help of statistical correlation analysis of a large pump-probe dataset. Overall, the joint response of the organic and metal layers leads to Fano-like spectral lineshapes at polariton energies. These findings are additionally supported by the analysis based on non-Hermitian Hamiltonian mechanics and *ab initio* transfer-matrix (TM) simulations. The approach described here is promising for attempts

to disentangle the response of polaritons from that of dark excitons in the organic layer and excitations in metal layers in optical microcavities paving the way towards better designs of optical-microcavity systems for their numerous future applications including sensing and energy-efficient organic-based photovoltaics.

Methods

Sample preparation

Fabry-Pérot cavities (Figure 1c) were prepared on glass substrates (AF32eco, Schott, 25x20x0.5 mm³) cleaned by sonication (10 minutes) in alkaline solution (Hellmanex), deionized water and 2-propanol. A fully reflective 100-nm bottom silver mirror was deposited by thermal evaporation. TIPS-PEN (6,13-Bis(triisopropylsilylethynyl)pentacene, Ossila Ltd.) and polystyrene (PS, Mw ca. 222k, Polymer Source Inc.) were used as received. To form the active layer, PS was first dissolved in toluene at a concentration of 20 mg.mL⁻¹. Then, TIPS-PEN was added to the solution to have a final relative mass ratio of 30%. Thin films were subsequently formed by spincoating and their thicknesses were adjusted by varying the spin speed (1800 and 2000 rpm for the thick and thin sample, respectively). The organic layer thicknesses of thin and thick cavities are 139 nm and 148 nm, respectively. The thin films were then annealed for 1 minute at 100°C to remove traces of residual solvent. The Fabry-Pérot cavities were closed by evaporating a 30 nm top silver mirror by thermal evaporation. Finally, a 50 nm protective encapsulation layer of aluminium oxide (AlO_x) was deposited on top of the cavity by atomic layer deposition (Ultratech, Savannah S100, precursor trimethyl-aluminium, Strem Chemicals, Inc.) at 80°C.

Angle-resolved steady-state reflectance spectroscopy

Absorption spectrum of TIPS-PEN/PS thin film was acquired with an Agilent Cary 6000i UV-Vis-NIR absorption spectrometer. Angle-resolved steady-state reflectance spectra of the

Fabry-Pérot cavities (Figure 1a-b) were acquired in a home-built Fourier microscopy setup²⁸ using a halogen light source (Ocean Optics, HL-2000-HP) focused onto the sample via an objective (60x, NA=0.9, Olympus, MPLAPON60X). The reflected light was imaged from the back focal plane of the objective onto the entrance slit of a spectrometer (Princeton Instruments IsoPlane SCT 320). A linear polarizer was used to select TE polarization. The resulting spectra were acquired with a Si-CCD camera (Princeton Instruments, PIXIS:400).

The angle-resolved steady-state reflectance spectra were fitted using a 3×3 coupled harmonic oscillator model to extract coupling strengths and Hopfield coefficients. Solving the following Hamiltonian leads to the polariton energy as eigenvalues, and the Hopfield coefficients as eigenvectors:

$$H = \begin{pmatrix} E_C(\theta) & V_\alpha & V_\beta \\ V_\alpha & E_\alpha & 0 \\ V_\beta & 0 & E_\beta \end{pmatrix}, \quad (1)$$

where E_α and E_β are the exciton energies, V_α and V_β are the coupling strengths for the corresponding transitions. The cavity energy E_C as a function of angle θ is given by:

$$E_C(\theta) = \frac{E_C(0)}{\sqrt{1 - \left(\frac{\sin \theta}{n_{eff}}\right)^2}} \quad (2)$$

with n_{eff} the effective refractive index.

Transient reflectance spectroscopy

Transient reflectance spectroscopy (shown schematically in Figure 1c) performed in this work is described elsewhere.²⁹ In a nutshell, an amplified Ti:Sapphire oscillator (Coherent Libra) produced 80 fs 1.55 eV optical pulses at 1 kHz. These in turn were split to drive a lab-built noncollinear optical parametric amplifier generating pump pulses (39 fs, 1.91 eV, 20 nJ, p-polarized), and CaF₂ white-light generator generating p-polarized probe pulses covering 1.65–2.88 eV. Differential reflectance

$$\frac{\Delta R}{R} = -\frac{R_{\text{ON}}(E, \tau) - R_{\text{OFF}}(E)}{R_{\text{OFF}}(E)} \quad (3)$$

was acquired, where R_{OFF} is reflectance of the probe beam from unperturbed sample, R_{ON} is that from the pumped sample, τ is pump-probe delay, E is detection energy. The resolution of the experiment was 100 fs.

Results

Strong coupling and polariton delocalization

Figures 1a,b show angle-resolved steady-state reflectance spectra of two cavities with different thicknesses with hybridized modes indicated. These modes are the consequence of strong coupling of excitons and photons giving rise to quasi-particles with intermediate effective mass referred to as exciton-polaritons or, simply, polaritons. The two lower polaritonic bands are assigned labels of UP and LP. Since bare excitonic bands (X_α and X_β) are not discernible in the strong coupling regime, they are referred here to as the bands of dark excitons, *i.e.*, excitons that have not coupled strongly to the cavity mode C . The amount of splitting between UP and LP at the bands' minima for the thin cavity (Figure 1a) is ~ 110 meV, whereas that for the thick cavity (Figure 1b) is ~ 100 meV. This difference in the interband splitting of hybridized states is likely a consequence of a larger detuning of the cavity mode from the main excitonic transition in thin cavity compared to that in thick cavity (Figures 1a,b). Coupling strength at a given angle is characterized by the Rabi energy, which generally only coincides with the interband polariton splitting in the regions where cavity mode crosses excitonic resonance. Such crossing between C and X_α never occurs in thin cavity (Figure 1a), therefore, a larger energy separation between UP and LP does not necessarily mean stronger coupling. There is a third polaritonic band present at ~ 2.1 eV, which is mostly excitonic in nature, and therefore not explicitly considered here.

More formally, these two significant polaritonic branches are the result of hybridization of diabatic states of exciton ($|\psi_{X_\alpha}\rangle$ and $|\psi_{X_\beta}\rangle$) and photon ($|\psi_C\rangle$),

$$|\psi_\pm\rangle = \sqrt{\alpha_\pm}|\psi_{X_\alpha}\rangle + \sqrt{\beta_\pm}|\psi_{X_\beta}\rangle + \sqrt{\gamma_\pm}|\psi_C\rangle, \quad (4)$$

Other, less intense, vibronic states also participate in hybridization, but their part is negligible and therefore omitted. In Eq. (4), $|\psi_\pm\rangle$ are UP (+) and LP (−) states; $\alpha_\pm, \beta_\pm, \gamma_\pm$ are

Hopfield coefficients defining how much there is excitonic ($\alpha_{\pm}, \beta_{\pm}$) and photonic (γ_{\pm}) contribution to a polaritonic branch (see Table 1 for excitonic and photonic contributions to UP and LP). Hopfield coefficients also define curvatures of hybridized modes in Figures 1a,b. We note that, in the case of thin cavity (Figure 1a), UP inherits larger photonic fraction compared to LP, whereas, in the case of thick cavity it is the LP band that is more photonic in nature than UP (see Supplementary material, Section S2, for estimations of Hopfield coefficients). The band with a greater degree of photonic nature also results in a larger absorption strength (Figure 1d) ultimately due to the cavity-facilitated local field enhancement effects²⁹ (see Supplementary material, Section S3, for local field simulations). This behaviour is similar to what was observed previously for amorphous rubrene.³⁰ The larger photonic field of a more photonic polariton also yields a stronger absorption at similar energies in metal layers within their penetration depth. This renders polaritons to be not only delocalized over the organic layer but also extended into the metal layers (as shown in Figure 1c) thus making them susceptible to the dynamics of both dark excitons and hot electrons.

Table 1: Excitonic ($\alpha + \beta$) and photonic (γ) contributions to UP and LP of thin and thick cavities, estimated from Hopfield coefficients averaged across the angles from -5° to 5° (see Supplementary material, Section S2).

	$\alpha + \beta$	γ
Thin cavity: UP	46%	54%
LP	71%	29%
Thick cavity: UP	69%	31%
LP	38%	62%

Pump-induced dynamics of strong-coupling conditions

To gain insights into the dynamics of strong coupling, transient reflectance experiments were carried out as shown in Figure 1c. Pump and probe beams arrive at nearly-normal-incidence angles so that it is the regions close to the bands' extrema in Figures 1a,b that were predominantly probed. The pump spectrum was tuned to overlap with the energy of uncoupled excitons X_{α} (Figure 1d) thus, in addition to polaritons and hot electrons, exciting the dark-

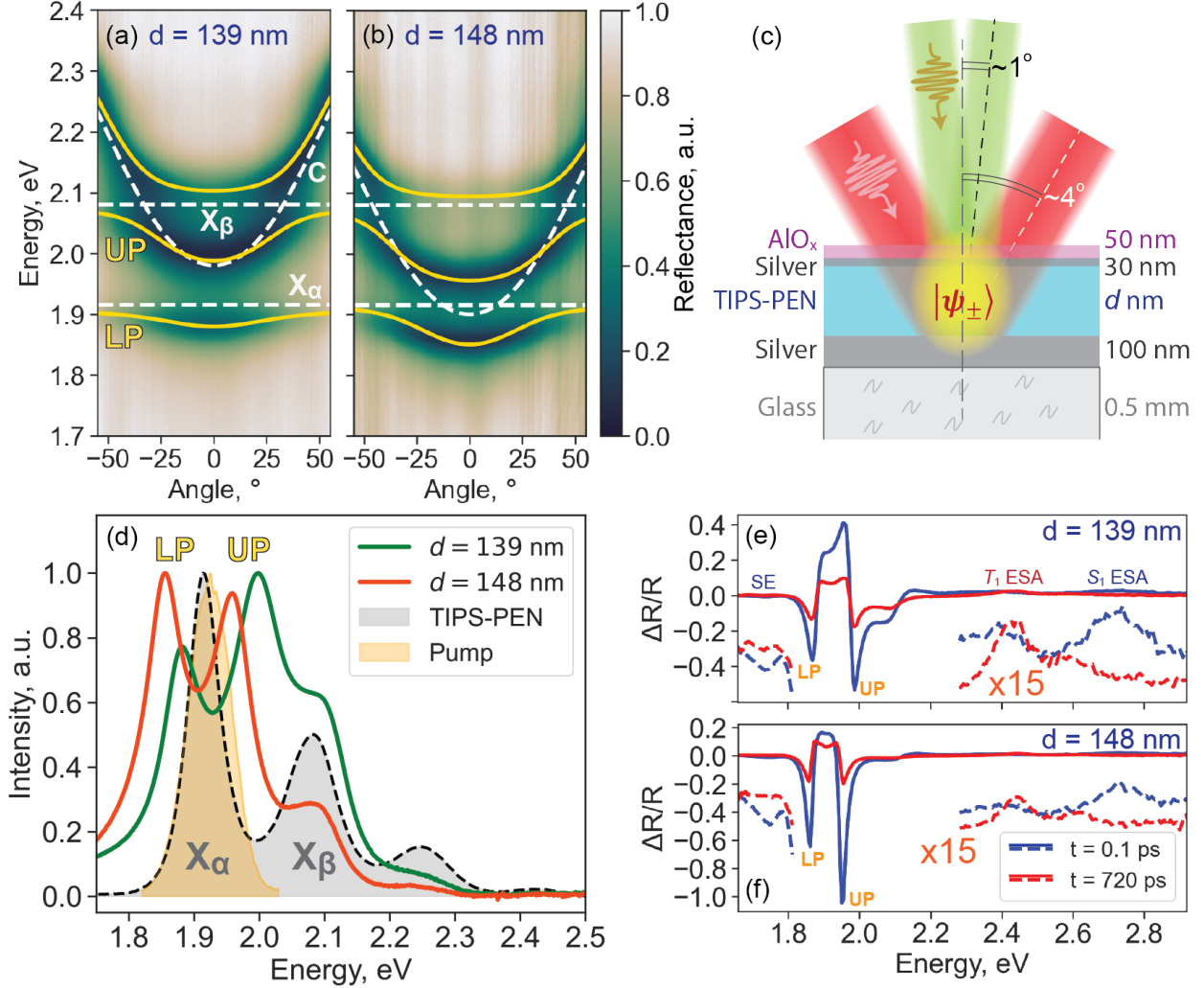


Figure 1: (a,b) Normalized angle-resolved steady-state reflectance spectra of (a) thin cavity ($d = 139$ nm) and (b) thick cavity ($d = 148$ nm), with the upper and lower polaritons (UP and LP), dark excitons (X_α and X_β), and cavity mode (C) indicated. Dashed lines represent diabatic excitonic (horizontal lines) and photonic (parabola) states; solid yellow lines represent hybridized adiabatic (polaritonic) states. (c) Schematics of the transient reflectance experiment. (d) Steady-state absorption spectra of thin (green) and thick (red) cavity, bare TIPS-PEN (dashed and shaded in grey), and pump spectrum (shaded in yellow). (e,f) Transient reflectance spectra at short (0.1 ps, blue) and long (720 ps, red) pump-probe delays of (e) thin and (f) thick cavity. The weak molecular response (dashed) is scaled by a factor of 15 and vertically offset for clarity.

states reservoir. Figures 1e,f show transient reflectance spectra from both samples acquired at short and long pump-probe delays (see Supplementary material, Section S4, for full transient maps). Notably, there is a long-lasting response at the energies of polaritonic bands,

which greatly dominates over the weak molecular response formed from stimulated emission (SE) in the lower-energy region ($\sim 1.7\text{--}1.8$ eV) and S_1/T_1 excited-state absorption (ESA) in the higher-energy region ($\sim 2.4\text{--}2.8$ eV). The latter corresponds to optical messengers of singlet fission in TIPS-PEN.²⁹ The polaritonic response is a doubly-dispersive lineshape (at ~ 1.92 eV), which has also been observed previously.^{13,24,27,31} One of the striking differences between thin and thick cavities is the weight of the loss (negative) signal at UP and LP energies at early pump-probe delays (< 10 ps): thick cavity features significant loss components (Figure 1f), which are less pronounced in the case of thin cavity (Figure 1e). At longer pump-probe delays (> 10 ps), these dramatic differences between the two samples vanish.

As also previously noticed, the lifetime of such response greatly exceeds expected lifetimes of both UP and LP. Indeed, the estimated cavity-mode lifetime in this study is $\tau_C \sim 9$ fs (cavities' Q-factor is ~ 45), so that polaritons' decay rate $\tau_{\pm}^{-1} = (\alpha_{\pm} + \beta_{\pm})\tau_X^{-1} + \gamma_{\pm}\tau_C^{-1} \gtrsim 30^{-1} \text{ fs}^{-1}$ falls far below the time-resolution of our experiments (~ 100 fs). Therefore polaritons are formed predominantly within the duration of pump and probe pulses and decay into the dark-states manifold within ~ 30 fs following ever-vanishing pulse tails. The pump pulses therefore effectively generate long-lived excitons in the organic layer and hot electrons in metal films; the probe pulses generate short-lived polaritons again, and it is these probe-induced polaritons that experience changing strong coupling conditions (due to excitations in the organic and metal layers). The difference in signals from pump-perturbed (R_{ON}) and unperturbed (R_{OFF}) samples results in long-lived dispersive lineshapes.

Discussion

Preliminary spectral analysis of the transient response using singular value decomposition (SVD, see Supplementary material, Section S5) and fittings with Fano formulae^{32–34} (see Supplementary material, Section S6) indicated that the measured transient spectra are inseparable in time and energy, so that an entangled spectro-temporal model taking into

account interference effects is necessary to describe strong coupling. Fano-based description additionally indicated the likely presence of a weak signal from dark excitons at ~ 1.92 eV overshadowed by the detected strong response at polaritonic energies. Altogether, the evolution of the extracted parameters resembled the course of singlet fission known to occur in TIPS-PEN suggesting that it is the dynamics of singlet and triplet excitons that modulated the polaritonic response simultaneously in energy and time.

We note that similar Fano-like lineshapes have been observed in various other systems where interference of either electromagnetic waves or probabilistic wavefunctions occurred.^{35–43} Most relevant to this work are induced transmission filters (ITFs),⁴³ where a strong dispersive $\Delta R/R$ response resulted from coupling of a highly-nonlinear 30-nm silver film to a Lorentz-like oscillator, thus revealing intrinsic strong nonlinearities in the metal layer. Such nonlinear effects of semi-transparent silver layers constituting thin and thick cavities considered here could also contribute to the measured overwhelming nonlinear response. The extracted time-varying Fano-parameters in this case would reflect net dynamics arising from contributions from both organic and metal layers.

Fano formulae provide information on the interband splitting of hybridized bands but not the Rabi energy. Therefore, in the next section a non-Hermitian formalism will be developed taking into account interference in the differential-reflectance domain, and thus describe entangled spectro-temporal behaviour of the strong response at the energies of UP and LP.

Singlet-fission dark excitons modulate strong coupling

A strongly-coupled exciton-photon system can be described by the following non-Hermitian Hamiltonian:

$$\mathbf{H} = \mathbf{E} + \mathbf{V} + \mathbf{\Gamma}, \quad (5)$$

$$\mathbf{E} = \begin{pmatrix} E_X & 0 \\ 0 & E_C \end{pmatrix}, \mathbf{V} = \begin{pmatrix} 0 & V \\ V^* & 0 \end{pmatrix}, \mathbf{\Gamma} = -\frac{i}{2} \begin{pmatrix} \Gamma_X & 0 \\ 0 & \Gamma_C \end{pmatrix}, \quad (6)$$

where \mathbf{E} contains the energies of effective exciton (E_X) and photon (E_C); \mathbf{V} describes coupling between them where $V = \hbar\Omega$ is the effective coupling strength, Ω is the Rabi frequency; and $\mathbf{\Gamma}$ describes decay rates for exciton (Γ_X) and photon (Γ_C). The eigenvectors of the unperturbed Hamiltonian \mathbf{E} are diabatic states of exciton ($|\psi_X\rangle$) and photon ($|\psi_C\rangle$). In the regime of their strong coupling, diagonalization of the Hamiltonian \mathbf{H} (Eq. (5)) yields steady-state eigenfunctions $|\psi_{\pm}\rangle$ and associated eigenenergies $\mathcal{E}_{\pm} = E_{\pm} - i\Gamma_{\pm}$ of two hybrid oscillators (UP, +, and LP, -), where E_{\pm} and Γ_{\pm} are their energies and widths, respectively. We note that although there are two vibronic resonances, X_{α} and X_{β} , contributing to polaritonic bands in our samples, they could be regarded as one effective exciton, which greatly simplifies analysis yet still allows for main trends to be extracted (see Supplementary material, Section S7, for the reduction of a 3D polaritonic state-vector to two dimensions). This is a reasonable simplification since the weight of X_{β} -exciton is smaller than the weight of X_{α} -exciton.

Since the measured dispersive lineshapes can be described with Fano formulae almost ideally (as noted above and shown in Supplementary material, Section S6), indicates that these lineshapes can be thought of as a result of interference of some kind. Therefore, two phase factors ϕ_{\pm} must enter the description of the two hybrid modes. Since we are interested in the changes of the parameters relative to the initial state (initiated by the pump pulse), we represent the state at any time instance after the pump excitation as a superposition of eigenfunctions of the Hamiltonian \mathbf{H} (Eq. (5)), *i.e.*,

$$|\psi\rangle = e^{i\phi_-} \cos \theta |\psi_- \rangle + e^{i\phi_+} \sin \theta |\psi_+ \rangle, \quad (7)$$

where θ controls weights of contributions from each of the polaritonic states, and ϕ_{\pm} were introduced to add relative phase offsets to the two states with respect to the global reference phase $\phi_0 = 0$ defined by the coupling elements in \mathbf{V} . Then, following the Green-function-

based approach,^{44–47} transient reflectance can be expressed as

$$\frac{\Delta R}{R} = -\frac{A}{\pi} \Im(G(E)), \text{ with } G = \frac{f_-}{E - \mathcal{E}_-} + \frac{f_+}{E - \mathcal{E}_+}, \quad (8)$$

where f_{\pm} are generalized differential oscillator strengths of the two polaritonic branches defined through c -products between the initial and final states,

$$f_{\pm} = (\psi|\psi_{\pm})(\psi_{\pm}|\psi); \quad (9)$$

and A is the scaling factor. We emphasize that since c -products (Eq. (9)) are used within the non-Hermitian framework, the phase factors of the polaritonic state-vectors enter the expressions for the oscillator strengths, and therefore nontrivial Fano-like resonances naturally appear within the framework. We also note that since Hamiltonian is non-Hermitian, the possibility for being in proximity to exceptional points (*i.e.*, the points where eigenvalues and eigenvectors coalesce) arises.³⁴ These singularities, or defects, were previously shown to lead to exotic behaviours including parity-time⁴⁸ or chiral⁴⁹ symmetry breaking, coherent perfect absorption,⁵⁰ enhanced sensitivity,⁵¹ photonic phase transitions,⁵² and exceptionally long lifetimes.^{53,54} The latter could potentially explain long lifetime of the observed polaritonic features, but we rule this possibility out by simply estimating the distances between UP/LP eigenvalues and eigenvectors which appear to remain far from zero for all pump-probe delays (see Supplementary material, Section S8, for the dynamics of eigenvalues and eigenvectors of thin and thick cavities).

Figure 2a illustrates intuition behind the introduced phases ϕ_{\pm} , which for this sake are remapped onto $\tilde{\phi}_{\pm} = (90^{\circ} + 2\phi_{\pm}) \bmod 180^{\circ}$. Specifically, the values of $\tilde{\phi}_{\pm}$ simply indicate the peak position of the reflectance spectrum R_{ON} relative to R_{OFF} in the intensity-energy domain. Thus, $\tilde{\phi}_{\pm} = 90^{\circ}$ corresponds to the loss (negative) signal indicating that R_{ON} spectrum is overall above R_{OFF} spectrum, whereas $\tilde{\phi}_{\pm} = -90^{\circ}$ corresponds to gain (positive) signal (R_{ON} spectrum is overall below R_{OFF} spectrum). The values of $\tilde{\phi}_{\pm} = 0^{\circ}, 180^{\circ}$ corre-

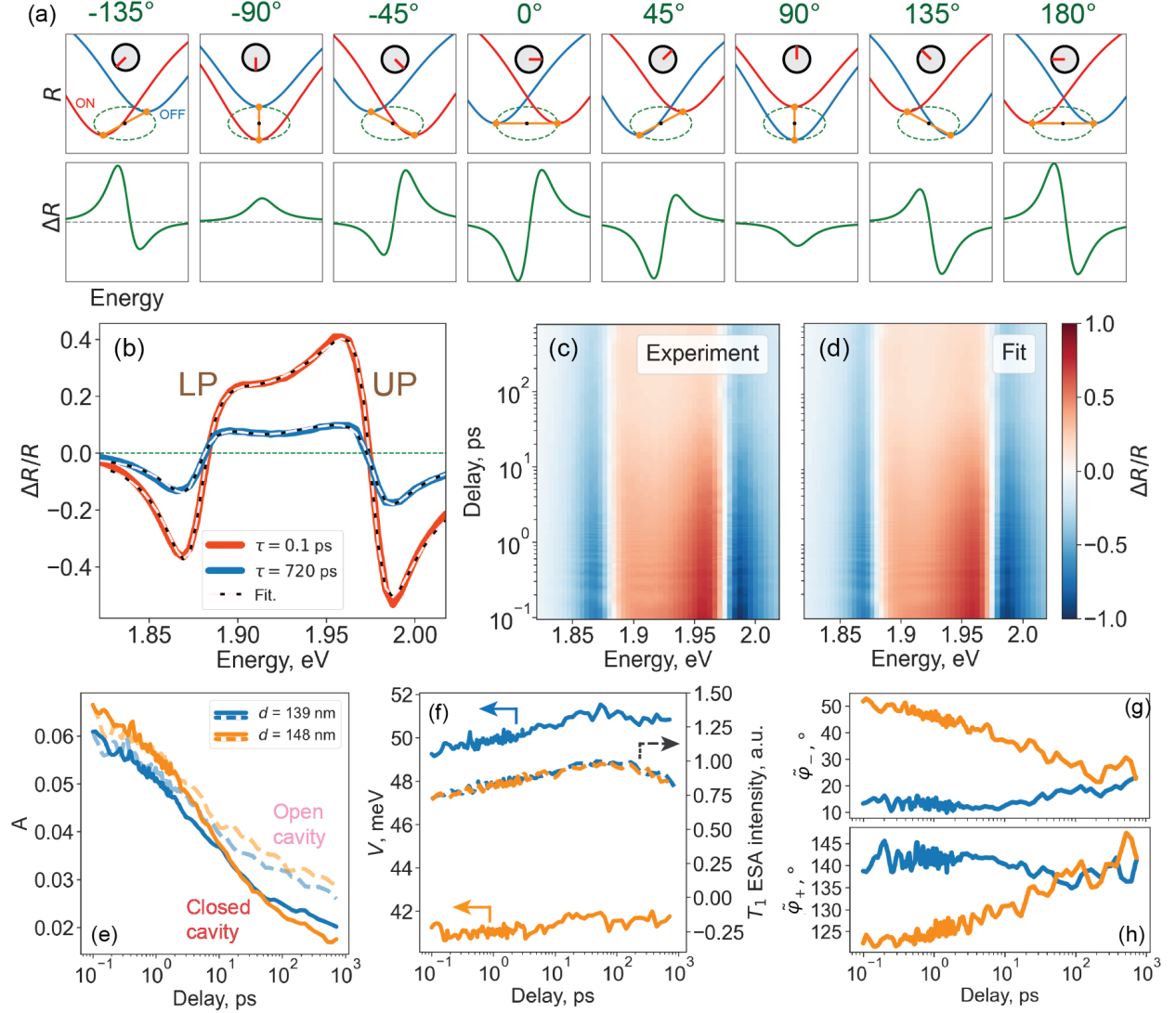


Figure 2: Non-Hermitian Hamiltonian description of transient reflectance spectra. (a) A cartoon explaining the physical meaning of the dynamic phases ϕ_{\pm} after remapping them onto more intuitive values $\tilde{\phi}_{\pm} = 90^{\circ} + 2\phi_{\pm}$ (modulo 180°). (upper row) "Pump-ON" (red) and "pump-OFF" (blue) reflectance spectra. The inset shows the phase $\tilde{\phi}$ and the direction of the offset of the "pump-ON" spectrum relative to the "pump-OFF" spectrum. (b) Fittings of short- and long-delay spectra for thin cavity. (c,d) Raw $\Delta R/R$ spectrum (c) and its corresponding fit (d) for thin cavity. (e–h) The scaling amplitude A (e, solid), coupling strengths V (f, solid), and phases $\tilde{\phi}_{\pm}$ (g,h) retrieved from fittings. In (e) dashed lines represent the absolute value of the bleach signal from the corresponding open cavities (*i.e.*, cavities without 30-nm metal film). In (f) dashed lines represent T_1 ESA signal from thin and thick cavities.

spond to more intense purely dispersive lineshapes. The intermediate values correspond to dispersive profiles with either negative or positive component dominating. The R_{ON} and

R_{OFF} peaks slide along the phase-ellipse around their average position. The shape of the ellipse is ultimately fixed by optical density of organic layer, pump fluence, and other experimental conditions, and its precise quantification falls beyond the scope of this work. We note that this qualitative picture is fully consistent with general cyclic correlation between phase ($\delta\phi$) and energy (δE) shifts, $\delta E \sim \cos \delta\phi$, for two classical harmonic oscillators.⁵⁵ Within our framework, the coupling strength V reflects only the average value between "pump-OFF" and "pump-ON" conditions. R_{OFF} spectrum, however, is time-independent, and therefore the dynamics of the Rabi energy V reflects the pump-induced dynamics encoded in the R_{ON} spectrum alone.

Figures 2b-h summarize fitting results using the described model. Figure 2b shows the fitting of the polaritonic response at short (0.1 ps) and long (720 ps) pump-probe delays. Provided the simplicity of the model, the fitting quality is remarkable. We point that overfitting is not the case here, since a minimum of eight parameters are needed to describe doubly-dispersive lineshapes (*e.g.*, energy, width, amplitude, and phase per spectral line) and there are exactly eight fitting parameters in our model (excluding a global scaling factor A). We have incorporated an additional parameter to describe the intensity of uncoupled excitons, thereby enhancing the accuracy of our model in the spectral region around 1.92 eV (see Supplementary material, Sections S9,10, for more details). Figures 2c,d compare experimental and fitted transient reflectance maps of strong polaritonic response demonstrating high fitting quality for all pump-probe delays. Applying global exponential fitting of the extracted parameters along the time axis revealed that the dynamics is characterized predominantly by four time constants similar to the case of bare film and open optical microcavities^{24,29} (*i.e.*, cavities without 30-nm metal film, see also Supplementary material, Section S11, for more details).

Figures 2e-h show evolution of some of the parameters (see Supplementary material, Section S10, for evolution of other parameters). The scaling factor A (Figure 2e) overall decays and in its dynamics resembles evolution of the main exciton bleach for the case of open

cavities, albeit with different time constants (*e.g.*, due to different photonic environment²⁹). This supports further that significant part of the polaritonic response originates from the dynamics of dark excitons. The exciton bleach dynamics is in turn correlated with the progression of singlet fission in which the amount of triplet excitons peaks on a sub-100 ps time scale. The dynamics of the Rabi energy V (Figure 2f) is also strongly correlated with the dynamics of dark triplet excitons occurring in accordance with singlet fission. We note that optical messengers of singlet fission and detected polaritonic response are energetically far from each other. Therefore, it is possible to enhance sensitivity at a selected spectral range towards physical phenomena that are otherwise more challenging to detect (*e.g.*, due to their weak nature or "inconvenient" energies) by simply tuning cavity resonance to overlap with correlated transitions that are more convenient for detection.

Notably, the phase offsets $\tilde{\phi}_{\pm}$ (Figures 2g,h) for the two samples evolve in opposite directions and converge to same values for long pump-probe delays where most of the initial excitations are relaxed and the dynamics is mostly governed by the dynamics of triplet excitons. Their values for UP and LP also lay on the opposite sides of the case of pure bleach-like spectrum ($\tilde{\phi}_{\pm} = 90^{\circ}$). Overall, the phase values and the direction of their evolution are in full agreement with the intuitive picture in Figure 2a, and indicate relaxation of the dispersive response towards a more symmetric lineshape with dominating loss components.

We note that the extracted phases should be considered as "effective", since they reflect combined dynamics occurring simultaneously in both organic and metal films. To gain insights into constitution of the observed lineshapes, we carried out *ab initio* electromagnetic simulations based on TM method,^{56,57} and a statistical correlation analysis of a large pump-probe dataset. In the next section, the mechanism behind solely dark excitons shaping the transient polaritonic response will be considered first, followed by description of effects from metal films.

Dark excitons add opposite phases to UP and LP

In our optical simulations, we introduce pump-induced changes to the refractive index of the organic layer, and retrieve local $\Delta R/R$ spectra (resolved along the optical axis) with the main goal to identify the effects of dark excitons. The choice of altering the refractive index (and not the extinction coefficient) is justified by its direct relation to the real part of pump-induced phase $\delta\phi(E) = \Re\left((\Delta n(E) + i\Delta\kappa(E))Ed/(\hbar c)\right)$ where $\Delta n(E) = n_{\text{ON}}(E) - n_{\text{OFF}}(E)$ is the change of the refractive index, $\Delta\kappa(E) = \kappa_{\text{ON}}(E) - \kappa_{\text{OFF}}(E)$ is the change of the absorption coefficient that is related to $\Delta n(E)$ through Kramers-Kronig relationship,^{58,59} and c is the speed of light in vacuum. Pump-induced refractive index n_{ON} of the molecular layer was defined as

$$n_{\text{ON}}(E) = \left[\delta_y \cdot (n_{\text{OFF}} - n_{\text{BG}}) + n_{\text{BG}} + \delta n_y \cdot n_{\text{BG}} \right] (\delta_x \cdot (E - E_X) + E_X + \delta E), \quad (10)$$

where the pump-induced changes are characterized by the four parameters δ_y , δn_y , δ_x , and δE : δ_y and δn_y introduce changes to the unperturbed refractive index n_{OFF} , whereas δ_x and δE introduce changes to its argument E . Parameters δ_x and δ_y stretch n_{OFF} relative to the dark-exciton energy $E_X = 1.914$ eV and refractive-index offset n_{BG} (estimated as mean value for the main exciton resonance), respectively. Such transformations correspond to the broadening of dark exciton spectrum and changes in the number of dark excitons, respectively. Parameters δn_y and δE introduce an offset to the refractive-index background (*e.g.*, due to changes in the properties of polystyrene matrix and/or metal layers) and shift of dark-exciton energy (as a fine-tuning mean), respectively.

Figures 3a–d summarize the effects of the four transformations of the refractive index additionally showing the sign of its change at UP and LP energies (see Supplementary material, Section S12, for more details on these simulations). It is clear that it is only changes in dark-exciton population and spectral broadening that are capable of introducing opposite phase offsets to UP and LP (Figures 3a,b), whereas the change in the refractive-index offset

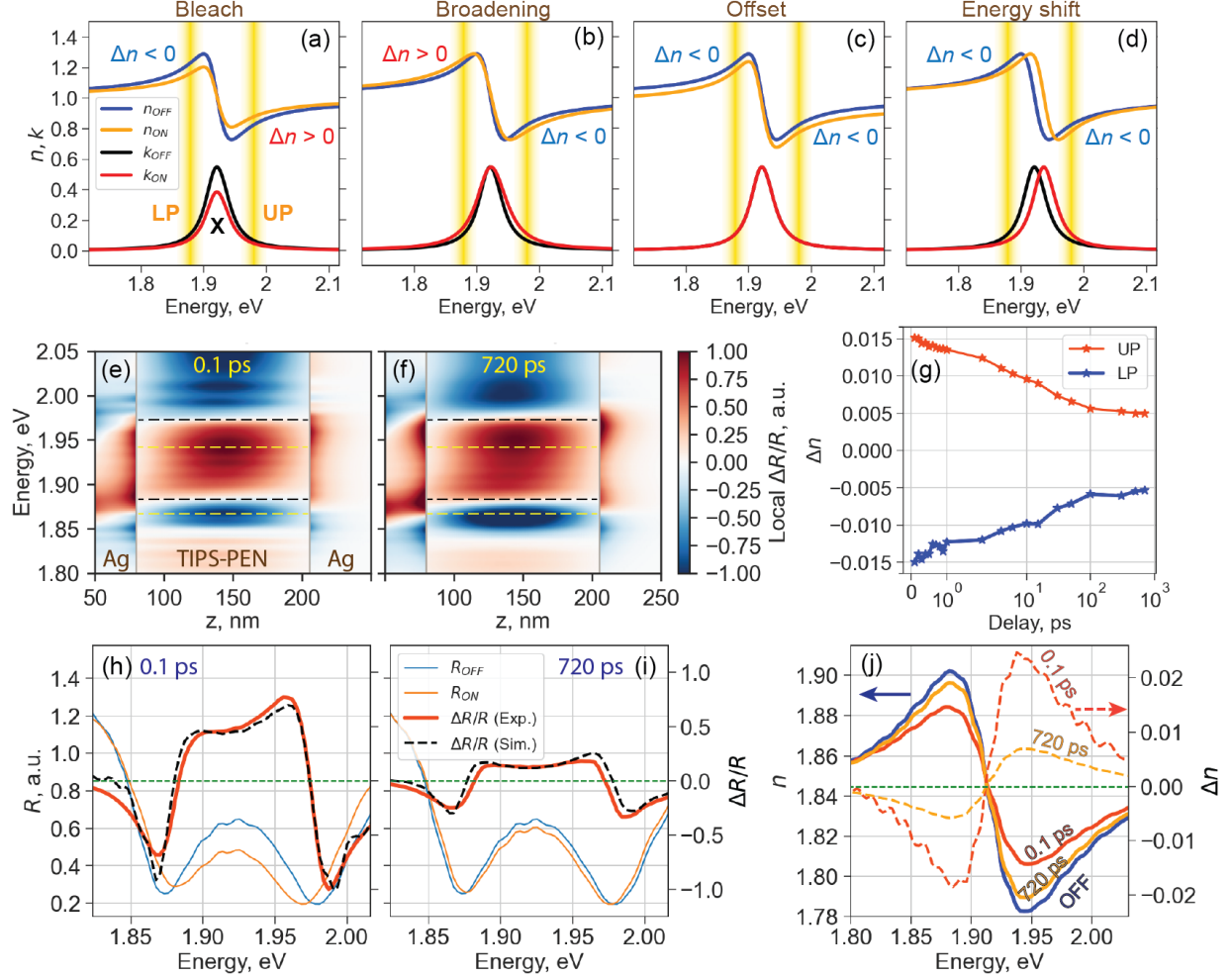


Figure 3: The effects of the dark-excitons' refractive-index (n) change (Δn) for thin cavity ($d = 139$ nm). (a–d) Cartoon explaining the action of Equation (10). (a) Scaling by a factor of 1.3 corresponding to the change in bleach of dark excitons; (b) broadening by a factor of 1.3; (c) refractive-index offset by -0.05 ; (d) energy shift by 15 meV. In the regions of normal dispersion, the signs of the refractive index change are indicated. (e, f) Normalized axially-resolved TM simulations of local $\Delta R/R$ spectra for (e) 0.1 and (f) 720 ps pump-probe delays. Metal (Ag) and organic (TIPS-PEN) layers are indicated. Dashed lines serve as references for convenience of the reader. (g) Time-resolved refractive-index changes of the organic layer at the energies of LP (blue) and UP (red). (h, i) TM fittings of experimental data together with the extracted R_{ON} and R_{OFF} spectra for pump-probe delays of (h) 0.1 ps and (i) 720 ps. (j) Time-resolved dynamics of the refractive index n of TIPS-PEN and its change Δn .

add phases of the same sign (Figure 3c). We note that in the latter case the change in the refractive-index offset alone would result in the double dispersive profile with the same sign of dispersiveness for both LP and UP, which was observed previously theoretically¹⁶ and experimentally.²⁷

Using Eq. (10), the measured $\Delta R/R$ spectra were fitted (using NSGA-II algorithm⁶⁰) with simulated spectra for multiple pump-probe delays. Two of the axially-resolved local $\Delta R/R$ spectra (at 0.1 and 720 ps) are shown in Figures 3e,f. The dispersive structures are present at the positions of UP and LP in the organic layer and extend into the metal layers in accordance with the Maxwell’s equations. Different optical properties of the metal films resulted in the local spectra distorted from ones in the organic layer with the net effect of mild shaping of axially-integrated $\Delta R/R$ lineshapes shown in Figures 3h,i. The splitting between UP and LP is observed to increase over time (see retrieved R_{ON} spectra) due to more excitons available for coupling to (probe) photons, the effect known as polariton contraction.^{61,62} Although the fitting quality is not as good as that based on Fano formulae and non-Hermitian Hamiltonian, it is still high provided only four fitting parameters. This is because TM-based description is intrinsically highly constrained by Maxwell’s equations, geometry of the problem, and optical properties of the materials. A poorer fitting quality indicates, as expected, that additional effects such as those originating from metal layers were not taken into account.

Figure 3g shows the dynamics of the refractive index of the organic layer at the energies of LP and UP (see Supplementary material, Section S13, for the dynamics of δ_x and δ_y). As a result of pump excitation the refractive index experienced by probe-induced LPs became lower, whereas that experienced by UPs increased, with both values relaxing towards unperturbed value at larger pump-probe delays. Figure 3j illustrates TM-retrieved refractive index of organic layer at the beginning and end of the measurement interval and its change with respect to the unperturbed dispersion qualitatively matching the case of dark-excitons-induced changes shown in Figure 3a (although broadening also took place). No prominent refractive-index offset was observed in the simulations resulting in discernible dispersive lineshapes of opposite signs at LP and UP energies.

We note that the extracted parameters describing refractive-index changes are overestimated since pump-induced optical effects of the metallic layers were not explicitly taken into

account: the dynamics in both organic and metal layers are embedded into the retrieved behaviour of the organic-layer’s refractive index. Nevertheless, since it was possible to fit reasonably well the measured response at multiple pump-probe delays with parameters related to solely dark excitons, we therefore conclude that dark excitons play a significant role in shaping detected polaritonic response. Next, we improve fitting quality of TM simulations by allowing metals to respond dynamically to the pump excitation, and finally identify the contribution from hot electrons using a statistical correlation analysis.

Metal layers contribute absorptive polaritonic response

Metals commonly exhibit orders of magnitude stronger nonlinearities amongst other materials, which can be accessed in thin metal films coupled to Lorentz-like oscillators⁴³ (polaritons in our case). This is possible because thin films not only reflect and absorb light, but also transmit a small fraction of it (due to finite penetration depth of electric field into metals^{63–65}) with the transmitted part carrying information on the dynamics of hot electrons. Hot electrons in metals are known to evolve in accordance with a two-temperature model with the majority of the dynamics occurring within the first time constant (~ 1 ps, electron-electron scattering) and the rest of the dynamics within the second time-constant (~ 10 ps, electron-phonon scattering).^{27,66} Transient optical response due to relaxation of hot electrons in turn could affect the penetration depth of metal mirrors and therefore the cavity optical length and position of the cavity mode as well as its bandwidth.⁶³ This would ultimately contribute additional transient phase offset between R_{ON} and R_{OFF} signals evolving together with electronic excitation in metal films. In this case, the two mirrors would generally contribute different phase offsets. Thus, for example, for an unperturbed case, the phase shift upon reflection from a 30-nm silver film at ~ 1.91 eV was estimated previously to be $\sim 140^\circ$, while for a 100-nm mirror the phase change was higher and similar to the bulk value.⁶⁵ Provided all these considerations, hot electrons are expected to imprint their evolution into the observed overwhelming response at the energies of UP and LP. It could be argued that

very small penetration depth would contribute only small signal to the axially-integrated response. However, small thickness of the silver's penetration depth is offset by its very large absorption coefficient thus enhancing absorptive response.

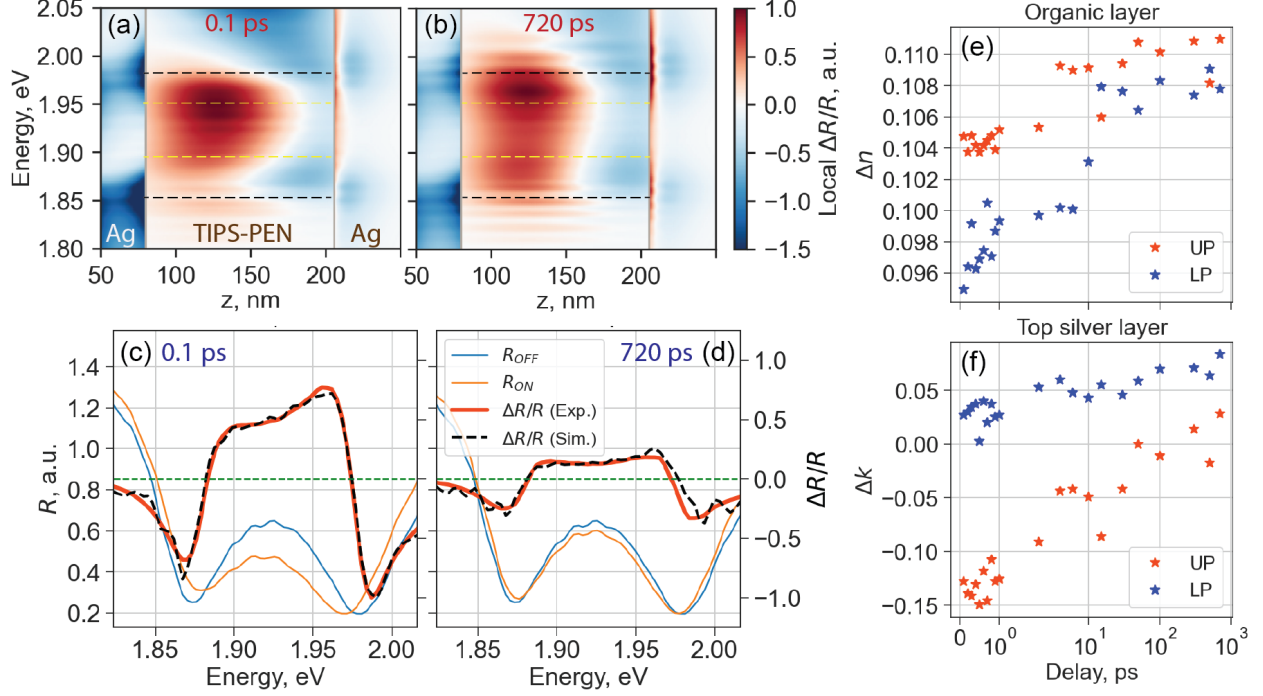


Figure 4: The effects of the metallic response for thin cavity ($d = 139$ nm). (a–d) Normalized axially-resolved TM simulations of (a,b) local and (c,d) integrated $\Delta R/R$ spectra for (a,c) 0.1 and (b,d) 720 ps pump-probe delays. In (a,b), metal (Ag) and organic (TIPS-PEN) layers are indicated. Dashed lines serve as references for convenience of the reader. In (c,d), reflectance spectra R_{ON} and R_{OFF} are also shown. (e,f) Changes of (e) refractive index of the organic layer and (f) extinction coefficient of the thin metal film versus pump-probe delay at the energies of LP (blue) and UP (red).

To take the effects of metal mirrors into account, we used the pump-induced refractive index changes of the organic layer extracted in the previous section to guide the optimization process, and let metal mirrors also respond to the optical excitation. Figures 4a,b show axially-resolved $\Delta R/R$ spectra at 0.1 ps and 720 ps. Within the organic layer, the general trend of increasing splitting between the positive peaks with pump-probe delays can be discerned similarly to the sole effect of dark excitons discussed above (Figures 3e,f). This indicates that dark excitons still contribute as before although to a lesser extent since the effects of metal layers have to be also accommodated. The negative components in this

case predominantly originated from metal layers, especially, from partially-transmitting 30-nm silver film ultimately giving rise to differential dispersive response at the energies of polaritonic branches (Figures 4c,d). These dispersive differential spectral profiles resemble the response from a 30-nm silver film reported previously,⁴³ and our results provide further insight into its origin.

Retrieved reflectance and differential reflectance spectra (Figures 4c,d) are similar to the ones in Figures 3h,i, but yielding a significantly improved fitting quality comparable to the quality of Fano-formulae- and non-Hermitian-Hamiltonian-based fittings. To check the sensibility of the retrieved reflectance spectra R_{ON} and R_{OFF} , we experimentally confirmed their behaviour at short and long pump-probe delays using similar cavities (see Supplementary material, Section S14).

We can now qualitatively relate made observations to the phases $\tilde{\phi}_{\pm}$ extracted from non-Hermitian description of polaritonic response. These phases correspond to net quantities containing the response of both metal ($\tilde{\phi}_{Ag,\pm} \sim 90^\circ$) and organic ($\tilde{\phi}_{\text{TIPS-PEN},-} \sim -45^\circ$ and $\tilde{\phi}_{\text{TIPS-PEN},+} \sim -135^\circ$) layers (see Figure 2a). Metals contribute mostly negative (loss) signal whereas organic layer contributes mostly positive (gain) signal.

Figures 4e,f show the dynamics of the refractive index of the organic layer and extinction coefficient of the thin metal film at the energies of UP and LP (other parameters did not show prominent dynamics) indicating that both organic and metal layers exhibit pump-induced dynamics. Due to the stochastic nature of optimization during TM-based fittings, however, there is large noise in the retrieved dynamics (Figure 4f), so that it is not possible to distinguish with certainty whether there are two time-constants corresponding to the dynamics of hot electrons. Therefore, to confirm their presence, we performed a more powerful statistical correlation analysis of a large pump-probe dataset aiming to identify signatures of a two-temperature model, which is described next.

An imprint of hot electrons in the polaritonic response

A large pump-probe dataset was additionally measured in a large variety of experimental conditions (Table 2) with the overall number of statistical samples equal to 150 (72 measurements on open cavities and 78 measurements on closed cavities). Each of the data-samples was split into two parts in energy-domain (Figure 5a): a high-energy part containing optical response from singlet and triplet excitons (*i.e.*, excitonic response) and a lower-energy part containing predominantly strong polaritonic response. From each of these parts time-constants were extracted via the global analysis of pump-probe spectra.^{29,67} The extracted time-constants were then correlated between excitonic and polaritonic responses separately for open and closed cavities (Figure 5b). Measurements on open optical microcavities served as a statistical reference.

Table 2: Experimental parameters and their value-ranges for statistical correlation analysis of measured data.

Parameter	Range of values
Cavity type	open, closed
Pump energy	X_α , X_β , LP, UP
Pump fluence	5–66 nJ
Cavity mode	1.71–1.98 eV

In the case of open cavities, as expected, average time constants (yellow markers) laid predominantly on the diagonal since lower- and higher-energy responses both corresponded to the dynamics of singlet and triplet excitons, and no polaritonic effects were in place. In the case of closed cavities, all three time constants (black markers) became shorter with the first two time-constants significantly deviating from the diagonal. We note that shorter time-constants in the closed cavities can result from the two effects: (*i*) Purcell effect²⁹ (which on its own would yield time-constants $\tau_{Purcell,i}$ $i = 1, 2, 3$), and (*ii*) hot electrons in silver metal relaxing in accordance with a two-temperature model (with time-constants $\tau_{Ag,i}$ $i = 1, 2$). The contribution of the latter effect to shortening of the time-constants is indeed possible since the first two time-constants (τ_i , $i = 1, 2$) measured in experiments are of the same order

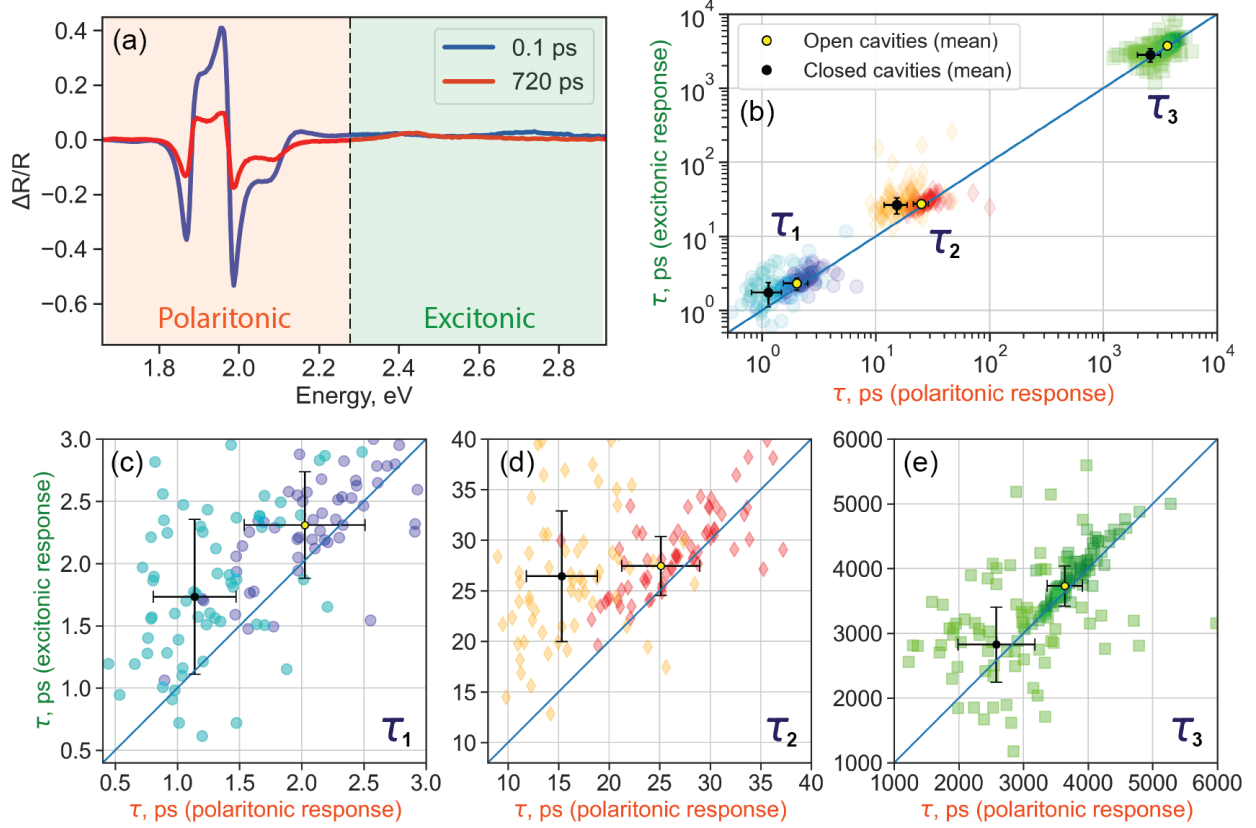


Figure 5: (a) Separation of transient spectra into polaritonic (shaded orange) and molecular (shaded green) response. (b–e) Correlation of time-constants extracted from molecular and polaritonic responses.

of magnitude as typical time-constants describing the dynamics of hot electrons in metals ($\tau_{Ag,1} \sim 1$ ps, $\tau_{Ag,2} \sim 10$ ps). Therefore the measured time-constants τ_i ($i = 1, 2$) reflect net values such that $\min(\tau_{Ag,i}, \tau_{Purcell,i}) < \tau_i < \max(\tau_{Ag,i}, \tau_{Purcell,i})$ (see Supplementary material, Section S15, for more details). The two effects, however, are possible to disentangle since the Purcell effect is characterized by time-independent local density of photonic states but not the real number of photons in the cavity, and therefore shortening of the three time-constants should be by a similar (if not the same) factor, whereas the effect of hot electrons is time-dependent. Indeed, Figures 5c–e show that the three time-constants are displaced horizontally by different amounts, with the first two time-constants being displaced to a greater extent than the third time-constant confirming contribution from hot electrons.

Conclusion

We investigated the polaritonic response from low-Q optical organic microcavities with TIPS-PEN and silver layers using steady-state and ultrafast-spectroscopy experiments. Non-Hermitian description of the detected response allowed us to conclude that the dynamics of the Rabi splitting was strongly correlated with singlet fission in the organic layer. Polaritons delocalized over both organic and metal layers were found to carry information on both dark excitons evolving in accordance with singlet fission and hot electrons evolving in accordance with a two-temperature model. The approach outlined in this study holds promise for endeavors to distinguish the pure polaritonic response from excitations in metal layers and subtle dark excitons in the active layer of low-Q optical microcavities. Our research outcomes carry significance for both the exploration and practical applications of manipulating photophysical and photochemical processes using photonics paving the way towards improved designs for optical organic microcavities to enhance control over these processes. This in turn is vital for the potential utilization of microcavities for various applications including energy-efficient organic-based photovoltaics. A more specific application is envisioned based on the observation that, due to small pump-induced changes to the Rabi energy, the response at long sub-ns pump-probe delays corresponds to the mathematical operation of differentiation of polaritonic spectra. This could be viewed as an alternative to analogue differentiation performed using ultrashort optical pulses, which could ultimately be exploited, *e.g.*, in polariton-based spatial light modulators⁶ for spectral differentiation of input beams as part of derivative-based analyses.^{68,69}

Acknowledgements

This research was funded by the Deutsche Forschungsgemeinschaft (DFG) via the Sonderforschungsbereich SFB 1249.

Authors disclosure statement

Authors declare no competing financial interests.

Supporting Information Available

The following file is available as Supplementary material:

Estimation of the organic-layer thickness and refractive index; Hopfield coefficients; Local electric fields; Transient differential reflectance spectra; SVD decomposition of pump-probe spectra; Fano resonances: a phenomenological description of transient polaritonic response; Reduction of 3D Hilbert space to two dimensions; Non-Hermitian Hamiltonian formalism; Non-Hermitian description of transient response; Non-Hermitian description of transient response with added bleach component; Global exponential fitting of the parameters; Lorentz-oscillator model of dielectric function and Kramers-Kronig relationship; Transfer-matrix simulations of transient reflectance; Experimental R_{OFF} and R_{ON} spectra; A comment on statistical correlation analysis of multiple pump-probe data.

References

1. Lee, A. J.; Spence, D. J.; Pask, H. M. Terahertz sources based on stimulated polariton scattering. *Progress in Quantum Electronics* **2020**, *71*, 100254.
2. Deng, H.; Weihs, G.; Snoke, D.; Bloch, J.; Yamamoto, Y. Polariton lasing vs. photon lasing in a semiconductor microcavity. *Proceedings of the National Academy of Sciences* **2003**, *100*, 15318–15323.
3. Ballarini, D.; Giorgi, M. D.; Cancellieri, E.; Houdré, R.; Giacobino, E.; Cingolani, R.; Bramati, A.; Gigli, G.; Sanvitto, D. All-optical polariton transistor. *Nature Communications* **2013**, *4*, 1778.
4. Xu, Y.; Wu, L.; Ang, L. Surface Exciton Polaritons: A Promising Mechanism for Refractive-Index Sensing. *Physical Review Applied* **2019**, *12*, 024029.
5. Nikolis, V. C.; Mischok, A.; Siegmund, B.; Kublitski, J.; Jia, X.; Benduhn, J.; Hör-

- mann, U.; Neher, D.; Gather, M. C.; Spoltore, D.; Vandewal, K. Strong light-matter coupling for reduced photon energy losses in organic photovoltaics. *Nature Communications* **2019**, *10*, 3706.
6. Jing-Quan, W.; Peng, H.; Jing-Lei, D.; Yong-Kang, G.; Xian-Gang, L.; Chun-Lei, D. Spatial Light Modulator Based on Surface Plasmon Polaritons for Chromatic Display. *Chinese Physics Letters* **2008**, *25*, 2908–2911.
 7. Ghosh, S.; Liew, T. C. H. Quantum computing with exciton-polariton condensates. *npj Quantum Information* **2020**, *6*, 16.
 8. Kasprzak, J.; Richard, M.; Kundermann, S.; Baas, A.; Jeambrun, P.; Keeling, J. M. J.; Marchetti, F. M.; Szymańska, M. H.; André, R.; Staehli, J. L.; Savona, V.; Littlewood, P. B.; Deveaud, B.; Dang, L. S. Bose–Einstein condensation of exciton polaritons. *Nature* **2006**, *443*, 409–414.
 9. Amo, A.; Lefrère, J.; Pigeon, S.; Adrados, C.; Ciuti, C.; Carusotto, I.; Houdré, R.; Giacobino, E.; Bramati, A. Superfluidity of polaritons in semiconductor microcavities. *Nature Physics* **2009**, *5*, 805–810.
 10. Nguyen, H.; Gerace, D.; Carusotto, I.; Sanvitto, D.; Galopin, E.; Lemaître, A.; Sagnes, I.; Bloch, J.; Amo, A. Acoustic Black Hole in a Stationary Hydrodynamic Flow of Microcavity Polaritons. *Physical Review Letters* **2015**, *114*, 036402.
 11. Hobson, P. A.; Barnes, W. L.; Lidzey, D. G.; Gehring, G. A.; Whittaker, D. M.; Skolnick, M. S.; Walker, S. Strong exciton–photon coupling in a low-Q all-metal mirror microcavity. *Applied Physics Letters* **2002**, *81*, 3519–3521.
 12. Pradeesh, K.; Baumberg, J. J.; Prakash, G. V. Strong exciton-photon coupling in inorganic-organic multiple quantum wells embedded low-Q microcavity. *Optics Express* **2009**, *17*, 22171.

13. Schwartz, T.; Hutchison, J. A.; Léonard, J.; Genet, C.; Haacke, S.; Ebbesen, T. W. Polariton Dynamics under Strong Light–Molecule Coupling. *ChemPhysChem* **2012**, *14*, 125–131.
14. Zhong, X.; Chervy, T.; Wang, S.; George, J.; Thomas, A.; Hutchison, J. A.; Devaux, E.; Genet, C.; Ebbesen, T. W. Non-Radiative Energy Transfer Mediated by Hybrid Light-Matter States. *Angewandte Chemie International Edition* **2016**, *55*, 6202–6206.
15. DelPo, C. A.; Kudisch, B.; Park, K. H.; Khan, S.-U.-Z.; Fassioli, F.; Fausti, D.; Rand, B. P.; Scholes, G. D. Polariton Transitions in Femtosecond Transient Absorption Studies of Ultrastrong Light–Molecule Coupling. *The Journal of Physical Chemistry Letters* **2020**, *11*, 2667–2674.
16. Renken, S.; Pandya, R.; Georgiou, K.; Jayaprakash, R.; Gai, L.; Shen, Z.; Lidzey, D. G.; Rao, A.; Musser, A. J. Untargeted effects in organic exciton–polariton transient spectroscopy: A cautionary tale. *The Journal of Chemical Physics* **2021**, *155*, 154701.
17. Hirai, K.; Hutchison, J. A.; Uji-i, H. Molecular Chemistry in Cavity Strong Coupling. *Chemical Reviews* **2023**, *123*, 8099–8126.
18. Quach, J. Q.; McGhee, K. E.; Ganzer, L.; Rouse, D. M.; Lovett, B. W.; Gauger, E. M.; Keeling, J.; Cerullo, G.; Lidzey, D. G.; Virgili, T. Superabsorption in an organic microcavity: Toward a quantum battery. *Science Advances* **2022**, *8*, eabk3160.
19. Ballarini, D.; Giorgi, M. D.; Gambino, S.; Lerario, G.; Mazzeo, M.; Genco, A.; Accorsi, G.; Giansante, C.; Colella, S.; D'Agostino, S.; Cazzato, P.; Sanvitto, D.; Gigli, G. Polariton-Induced Enhanced Emission from an Organic Dye under the Strong Coupling Regime. *Advanced Optical Materials* **2014**, *2*, 1076–1081.
20. Wang, M.; Hertzog, M.; Börjesson, K. Polariton-assisted excitation energy channeling in organic heterojunctions. *Nature Communications* **2021**, *12*, 1874.

21. Martínez-Martínez, L. A.; Du, M.; Ribeiro, R. F.; Kéna-Cohen, S.; Yuen-Zhou, J. Polariton-Assisted Singlet Fission in Acene Aggregates. *The Journal of Physical Chemistry Letters* **2018**, *9*, 1951–1957.
22. Polak, D.; Jayaprakash, R.; Lyons, T. P.; Martínez-Martínez, L. Á.; Leventis, A.; Fallon, K. J.; Coulthard, H.; Bossanyi, D. G.; Georgiou, K.; Anthony J. Petty, I.; Anthony, J.; Bronstein, H.; Yuen-Zhou, J.; Tartakovskii, A. I.; Clark, J.; Musser, A. J. Manipulating molecules with strong coupling: harvesting triplet excitons in organic exciton microcavities. *Chemical Science* **2020**, *11*, 343–354.
23. Du, M.; Martínez-Martínez, L. A.; Ribeiro, R. F.; Hu, Z.; Menon, V. M.; Yuen-Zhou, J. Theory for polariton-assisted remote energy transfer. *Chemical Science* **2018**, *9*, 6659–6669.
24. Liu, B.; Menon, V. M.; Sfeir, M. Y. The Role of Long-Lived Excitons in the Dynamics of Strongly Coupled Molecular Polaritons. *ACS Photonics* **2020**, *7*, 2292–2301.
25. Gu, B.; Mukamel, S. Optical-Cavity Manipulation of Conical Intersections and Singlet Fission in Pentacene Dimers. *The Journal of Physical Chemistry Letters* **2021**, *12*, 2052–2056.
26. Climent, C.; Casanova, D.; Feist, J.; Garcia-Vidal, F. J. Not dark yet for strong light-matter coupling to accelerate singlet fission dynamics. *Cell Reports Physical Science* **2022**, *3*, 100841.
27. Liu, B.; Menon, V. M.; Sfeir, M. Y. Ultrafast thermal modification of strong coupling in an organic microcavity. *APL Photonics* **2021**, *6*, 016103.
28. Graf, A.; Tropf, L.; Zakharko, Y.; Zaumseil, J.; Gather, M. C. Near-infrared exciton-polaritons in strongly coupled single-walled carbon nanotube microcavities. *Nature Communications* **2016**, *7*, 13078.

29. Kolesnichenko, P. V.; Hertzog, M.; Hainer, F.; Deschler, F.; Zaumseil, J.; Buckup, T. *submitted* **2023**,
30. Takahashi, S.; Watanabe, K.; Matsumoto, Y. Singlet fission of amorphous rubrene modulated by polariton formation. *The Journal of Chemical Physics* **2019**, *151*, 074703.
31. Xiang, B.; Ribeiro, R. F.; Li, Y.; Dunkelberger, A. D.; Simpkins, B. B.; Yuen-Zhou, J.; Xiong, W. Manipulating optical nonlinearities of molecular polaritons by delocalization. *Science Advances* **2019**, *5*, eaax5196.
32. Fano, U. Effects of Configuration Interaction on Intensities and Phase Shifts. *Physical Review* **1961**, *124*, 1866–1878.
33. Limonov, M. F.; Rybin, M. V.; Poddubny, A. N.; Kivshar, Y. S. Fano resonances in photonics. *Nature Photonics* **2017**, *11*, 543–554.
34. Caselli, N.; Intonti, F.; China, F. L.; Biccari, F.; Riboli, F.; Gerardino, A.; Li, L.; Linfield, E. H.; Pagliano, F.; Fiore, A.; Gurioli, M. Generalized Fano lineshapes reveal exceptional points in photonic molecules. *Nature Communications* **2018**, *9*, 396.
35. Lin, M.-F.; Pfeiffer, A. N.; Neumark, D. M.; Leone, S. R.; Gessner, O. Strong-field induced XUV transmission and multiplet splitting in $4d^{-1}6p$ core-excited Xe studied by femtosecond XUV transient absorption spectroscopy. *The Journal of Chemical Physics* **2012**, *137*, 244305.
36. Liao, C.-T.; Sandhu, A. XUV Transient Absorption Spectroscopy: Probing Laser-Perturbed Dipole Polarization in Single Atom, Macroscopic, and Molecular Regimes. *Photonics* **2017**, *4*, 17.
37. Levi, F.; Camparo, J.; Francois, B.; Calosso, C. E.; Micalizio, S.; Godone, A. Precision test of the ac Stark shift in a rubidium atomic vapor. *Physical Review A* **2016**, *93*, 023433.

38. Barontini, G.; Blackburn, L.; Boyer, V.; Butuc-Mayer, F.; Calmet, X.; López-Urrutia, J. R. C.; Curtis, E. A.; Darquié, B.; Dunningham, J.; Fitch, N. J.; Forgan, E. M.; Georgiou, K.; Gill, P.; Godun, R. M.; Goldwin, J.; Guarrera, V.; Harwood, A. C.; Hill, I. R.; Hendricks, R. J.; Jeong, M. *et al.* Measuring the stability of fundamental constants with a network of clocks. *EPJ Quantum Technology* **2022**, *9*, 12.
39. Salikhov, K. M. Consistent Paradigm of the Spectra Decomposition into Independent Resonance Lines. *Applied Magnetic Resonance* **2016**, *47*, 1207–1227.
40. Mun, S.-E.; Yun, H.; Choi, C.; Kim, S.-J.; Lee, B. Enhancement and Switching of Fano Resonance in Metamaterial. *Advanced Optical Materials* **2018**, *6*, 1800545.
41. Qi, J.; Chen, Z.; Chen, J.; Li, Y.; Qiang, W.; Xu, J.; Sun, Q. Independently tunable double Fano resonances in asymmetric MIM waveguide structure. *Optics Express* **2014**, *22*, 14688.
42. Zhang, T.; Zhang, D.; Zhang, H.-F. Realization of double Fano resonances with a InSb-doped Fabry-Perot cavity. *Results in Physics* **2022**, *35*, 105417.
43. Owens, D. T.; Fuentes-Hernandez, C.; Hales, J. M.; Perry, J. W.; Kippelen, B. Nonlinear optical properties of induced transmission filters. *Optics Express* **2010**, *18*, 19101.
44. Moiseyev, N.; Certain, P.; Weinhold, F. Resonance properties of complex-rotated hamiltonians. *Molecular Physics* **1978**, *36*, 1613–1630.
45. Kukulin, V. I.; Krasnopol'sky, V. M.; Horáček, J. *Theory of Resonances*; Springer Netherlands, 1989.
46. Durand, P.; Paidarová, I.; Gadéa, F. X. Theory of Fano profiles. *Journal of Physics B: Atomic, Molecular and Optical Physics* **2001**, *34*, 1953–1966.
47. Paidarová, I.; Durand, P. Quantum Resonances: Line Profiles and Dynamics. *Collection of Czechoslovak Chemical Communications* **2003**, *68*, 529–553.

48. Wen, J.; Jiang, X.; Jiang, L.; Xiao, M. Parity-time symmetry in optical microcavity systems. *Journal of Physics B: Atomic, Molecular and Optical Physics* **2018**, *51*, 222001.
49. Heiss, W.; Harney, H. The chirality of exceptional points. *The European Physical Journal D* **2001**, *17*, 149–151.
50. Wang, C.; Sweeney, W. R.; Stone, A. D.; Yang, L. Coherent perfect absorption at an exceptional point. *Science* **2021**, *373*, 1261–1265.
51. Hodaei, H.; Hassan, A. U.; Wittek, S.; Garcia-Gracia, H.; El-Ganainy, R.; Christodoulides, D. N.; Khajavikhan, M. Enhanced sensitivity at higher-order exceptional points. *Nature* **2017**, *548*, 187–191.
52. Öztürk, F. E.; Lappe, T.; Hellmann, G.; Schmitt, J.; Klaers, J.; Vewinger, F.; Kroha, J.; Weitz, M. Observation of a non-Hermitian phase transition in an optical quantum gas. *Science* **2021**, *372*, 88–91.
53. Dietz, B.; Friedrich, T.; Metz, J.; Miski-Oglu, M.; Richter, A.; Schäfer, F.; Stafford, C. A. Rabi oscillations at exceptional points in microwave billiards. *Physical Review E* **2007**, *75*, 027201.
54. Heiss, W. D. Time behaviour near to spectral singularities. *The European Physical Journal D* **2010**, *60*, 257–261.
55. Tolmachev, A. V.; Masselon, C. D.; Anderson, G. A.; Udseth, H. R.; Smith, R. D. Frequency shifts due to the interference of resolved peaks in magnitude-mode Fourier-transform ion cyclotron resonance mass spectra. *Journal of the American Society for Mass Spectrometry* **2002**, *13*, 387–401.
56. Pettersson, L. A. A.; Roman, L. S.; Inganäs, O. Modeling photocurrent action spectra of photovoltaic devices based on organic thin films. *J. Appl. Phys.* **1999**, *86*, 487–496.
57. Hecht, E. *Optics, Global Edition*; Pearson, 2016.

58. de L. Kronig, R. On the Theory of Dispersion of X-Rays. *Journal of the Optical Society of America* **1926**, *12*, 547.
59. Toll, J. S. Causality and the Dispersion Relation: Logical Foundations. *Physical Review* **1956**, *104*, 1760–1770.
60. Deb, K.; Pratap, A.; Agarwal, S.; Meyarivan, T. A fast and elitist multiobjective genetic algorithm: NSGA-II. *IEEE Transactions on Evolutionary Computation* **2002**, *6*, 182–197.
61. Dunkelberger, A. D.; Davidson, R. B.; Ahn, W.; Simpkins, B. S.; Owrutsky, J. C. Ultrafast Transmission Modulation and Recovery via Vibrational Strong Coupling. *The Journal of Physical Chemistry A* **2018**, *122*, 965–971.
62. Xiang, B.; Ribeiro, R. F.; Chen, L.; Wang, J.; Du, M.; Yuen-Zhou, J.; Xiong, W. State-Selective Polariton to Dark State Relaxation Dynamics. *The Journal of Physical Chemistry A* **2019**, *123*, 5918–5927.
63. Becker, H.; Burns, S. E.; Tessler, N.; Friend, R. H. Role of optical properties of metallic mirrors in microcavity structures. *Journal of Applied Physics* **1997**, *81*, 2825–2829.
64. Black, C.; Welser, J. Electric-field penetration into metals: consequences for high-dielectric-constant capacitors. *IEEE Transactions on Electron Devices* **1999**, *46*, 776–780.
65. Ma, F.; Liu, X. Phase shift and penetration depth of metal mirrors in a microcavity structure. *Applied Optics* **2007**, *46*, 6247.
66. Temnov, V. V.; Nelson, K. A.; Armelles, G.; Cebollada, A.; Thomay, T.; Leitenstorfer, A.; Bratschitsch, R. Femtosecond surface plasmon interferometry. *Optics Express* **2009**, *17*, 8423.

67. van Stokkum, I. H.; Larsen, D. S.; van Grondelle, R. Global and target analysis of time-resolved spectra. *Biochimica et Biophysica Acta (BBA) - Bioenergetics* **2004**, *1657*, 82–104.
68. Zangeneh-Nejad, F.; Souнас, D. L.; Alù, A.; Fleury, R. Analogue computing with meta-materials. *Nature Reviews Materials* **2020**, *6*, 207–225.
69. Dubrovkin, J. *Derivative spectroscopy*; Cambridge Scholars Publishing, 2021.